







Chaotic escape of impurities and sticky orbits in toroidal plasmas

L. C. Souza ^{1,*} M. R. Sales ² M. Mugnaine ³ J. D. Szezech, Jr. ² I. L. Caldas ³ and R. L. Viana ^{1,3}

¹Universidade Federal do Paraná, Departamento de Física, Curitiba, PR 81531-990, Brazil

²Universidade Estadual de Ponta Grossa, Programa de Pós-Graduação em Ciências, Ponta Grossa, PR 84030-900, Brazil

³Universidade de São Paulo, Instituto de Física, São Paulo, SP 05315-970, Brazil



(Received 12 September 2023; accepted 1 December 2023; published 5 January 2024)

We investigate chaotic impurity transport in toroidal fusion plasmas (tokamaks) from the point of view of passive advection of charged particles due to $\mathbf{E} \times \mathbf{B}$ drift motion. We use realistic tokamak profiles for electric and magnetic fields as well as toroidal rotation effects, and consider also the effects of electrostatic fluctuations due to drift instabilities on particle motion. A time-dependent one degree-of-freedom Hamiltonian system is obtained and numerically investigated through a symplectic map in a Poincaré surface of section. We show that the chaotic transport in the outer plasma region is influenced by fractal structures that are described in topological and metric point of views. Moreover, the existence of a hierarchical structure of islands-around-islands, where the particles experience the stickiness effect, is demonstrated using a recurrence-based approach.

DOI: [10.1103/PhysRevE.109.015202](https://doi.org/10.1103/PhysRevE.109.015202)

I. INTRODUCTION

The transport of impurities in fusion reactor plasmas has been the object of many theoretical, computational, and experimental investigations [1]. These impurities can be charged particles created from plasma-wall interactions in tokamaks, for example [2]. The transport of such impurities raise a number of key issues in both physical and technological levels. In ITER (International Thermonuclear Experimental Reactor), for example, that is expected to produce 500 MW of fusion power [3,4], particle transport (not just impurities) may generate heat loads of 5–10 MW/m² that can damage the tokamak inner wall [5]. In order to mitigate this problem, both in ITER as well as in other tokamaks like JET and Alcator C-Mod, divertor concepts have been proposed so as to capture or divert energetic particles escaping from the plasma [6–8].

Divertors are shaped metallic plates placed outside the plasma boundary, and particles can be deviated so as to hit them by magnetic field lines connecting the outer portion of the plasma column and the inner wall. However, if particle fluxes are too large even the divertor plates can be damaged, so chaotic magnetic field lines have been proposed to uniformize heat and particle loadings [9]. These chaotic field lines can be produced, for example, by the application of suitable external magnetic fields. When combined with the equilibrium field, the resulting field lines can form a cold chaotic boundary layer insulating the wall (and the divertors) from the plasma core. The latter is the so-called ergodic divertor concept, realized with resonant helical windings [10] or current rings of finite length [11].

A fundamental question in the successful operation of ergodic divertors is how uniform are the heat and particle loadings on the plates, the so-called magnetic footprints. Experimental results show that these loadings are not really

uniform, but that magnetic footprints seem to have a self-similar organization, a fractal pattern indeed [12]. Magnetic field line models using nonintegrable Hamiltonian systems are able to show that these fractal patterns are ultimately related to some topological structures underlying chaotic, area-filling orbits, in a Poincaré surface of section [13–15]. This point of view has been intensively investigated by Evans and his collaborators in a number of seminal papers on the subject [16,17].

In this paper, we shall pursue another pathway to describe chaotic impurity transport in toroidal plasmas, by including electrostatic fluctuations in the model equations. The magnetic confinement of toroidal plasmas in machines like tokamaks and stellarators is strongly affected by a large number of instabilities. Among them, one of the most important is represented by drift instabilities, occurring when there are steep density gradients in the plasma column. They are commonly observed in plasmas of nonuniform density that are kept in equilibrium by a dominant magnetic field, which gives to such instabilities an universal character [18,19].

In the case of low frequencies, the magnetic perturbations play essentially no role and drift waves are electrostatic, in the sense that the electric field points along the propagation direction and $\nabla \times \tilde{\mathbf{E}} = \mathbf{0}$, enabling us to define a potential [20] such that $\tilde{\mathbf{E}} = -\nabla\tilde{\phi}$. The electrostatic field associated with drift wave, combined with the dominant magnetic field, produces a $\mathbf{E} \times \mathbf{B}$ drift in particle motion. In addition, plasma turbulence in tokamaks is dominated by $\mathbf{E} \times \mathbf{B}$ drift effects [21].

The drift equations of motion can be made even more realistic by including radial profiles of equilibrium quantities related to electromagnetic fields, and which are ingredients of modern tokamak scenarios. The resulting model, proposed by Horton [20], has a Hamiltonian character, being a nonautonomous one-and-a-half degrees of freedom system. By defining action-angle variables in a suitably chosen Poincaré surface of section, one can describe the motion of particles

*Corresponding author: leonardo@fisica.ufpr.br

using a two-dimensional area-preserving map. Being nonintegrable, it is possible to describe chaotic motion in a region that extends from the outer plasma column to the tokamak wall.

Our strategy is to describe the diffusion of impurities using this model, by assuming that they are passive particles, i.e., they suffer the influence of the electric and magnetic fields but they do not alter these fields in a significant way. Hence impurity particles behave as passive tracers, being advected by the $\mathbf{E} \times \mathbf{B}$ flow in a similar way as dye particles are advected by incompressible flows in two spatial dimensions. The incompressibility condition, in the plasma context, is provided by Liouville's theorem, which is also responsible by the area-preserving nature of the discrete-time map in the Poincaré surface of section. We also assume that the density of impurities is so low that particles can be described individually, neglecting collisional effects. A more comprehensive description of impurity transport, considering larger particle densities, would require more sophisticated models that use kinetic and/or fluid descriptions to investigate this problem from the point of view of neoclassical and anomalous transport [1].

In this paper, we aim to explore some dynamical properties of the chaotic impurity transport using Horton's model endowed with radial profiles obtained in agreement with experimental data obtained in the TCABR tokamak, operating in the Institute of Physics of São Paulo University. This type of model has a built-in mechanism of chaotic dynamics generation, which is just the presence of electrostatic fluctuations, which are strictly deterministic. In principle, at least, there is no need of adding stochastic noisy terms. Moreover, there is no external magnetic field like in ergodic divertors, which simplifies the physical setting in a considerable way.

Our main goal is to apply concepts from nonlinear dynamics to characterize chaotic transport as a passive advection problem. Since we are dealing with particle escape (after a number of them collide with the inner tokamak wall) this is an open Hamiltonian system. Chaotic orbits in open Hamiltonian systems have been investigated for a long time, including the hydrodynamical analog of our system. The dynamics of chaotic orbits in phase space is governed by the properties of an invariant, nonattracting chaotic set (chaotic saddle) and its corresponding invariant manifold structure. We interpret the nonuniformity of passive particle transport in terms of the dynamics around a chaotic saddle, describing the motion using dynamical tools like Lyapunov exponents, fractal dimensions, and escape rates. These diagnostics form a useful toolbox that can be used to describe virtually any other situation in which passive particle advection is investigated. Moreover, the chaotic particle may be trapped in a complex structure around the islands, given rise to the stickiness effect [22]. This affects transport and statistical properties of chaotic orbits, the trajectories, which would otherwise freely explore all chaotic regions of phase space, find themselves temporally confined to a peculiar quasiperiodic motion within the vicinity of islands, thus having a large kinetic energy. In this paper, we used the finite-time recurrence time entropy [23], a method based on recurrences that allow us to detect sticky orbits without the need for calculating the Jacobian matrix.

We find that the chaotic saddle is almost a area filling curve with box-counting dimension and information

dimension close to the dimension of the phase space. With the recurrence time entropy, it is possible to discern the fine structure of stickiness by identifying a multi-modal distribution, in which each maximum is related to a different hierarchical level in the islands-around-islands structure. Furthermore, these regions exhibit a power-law decay pattern in the cumulative distribution of trapping times.

The paper is organized as follows: In Sec. II we outline the derivation of the symplectic map describing drift particle motion in tokamaks with drift instabilities and sheared radial profiles for electric and magnetic fields, as well as toroidal velocity. Basic dynamical properties of the map are briefly described, with focus on the formation of a boundary layer of chaotic motion near the tokamak wall. In Sec. III we focus on the chaotic saddle underlying motion in the chaotic orbit. Section IV considers the physical consequences of fractality on observable dynamical quantities like the escape rate. The connection among the latter with Lyapunov exponents and fractal dimensions are revisited. Section V uses the concept of recurrence time entropy, showing how it can reveal trapping structures in the chaotic region causing stickiness of motion, which influences the numerical computation of diffusion in action variable. The last section contains our conclusions.

II. SYMPLECTIC MAP FOR $\mathbf{E} \times \mathbf{B}$ DRIFT MOTION

In the present model we use local coordinates (r, θ, φ) to indicate the position of passive particles, where r is measured from the minor axis, θ is the poloidal angle, and φ the toroidal angle. Denoting by a and R_0 the minor and major radius, respectively, in the large aspect ratio approximation ($\epsilon = a/R_0 \ll 1$), the equilibrium magnetic field is $\mathbf{B} = (0, B_\theta(r), B_\varphi)$, where B_φ and $B_\theta \sim \epsilon B_\varphi$ are the toroidal and poloidal components, respectively, such that $B \approx B_\varphi \gg B_\theta$. Hence the magnetic surfaces are described by the safety factor $q(r) = rB/R_0B_\theta(r)$.

On analyzing the $\mathbf{E} \times \mathbf{B}$ drift motion of passive particles, the electrostatic field will be given as

$$\mathbf{E} = E_r(r)\hat{\mathbf{r}} - \nabla\tilde{\phi}(r, \theta, \varphi; t), \quad (1)$$

where E_r is an external radial field and $\tilde{\phi}$ represent electrostatic drift instabilities. Adding a toroidal velocity v_\parallel , with a specified radial profile, the drift equations of motion read, in local coordinates,

$$\frac{dr}{dt} = -\frac{1}{rB} \frac{\partial\tilde{\phi}}{\partial\theta}, \quad (2)$$

$$\frac{d\theta}{dt} = \frac{v_\parallel(r)}{R_0q(r)} - \frac{E_r(r)}{rB} + \frac{1}{rB} \frac{\partial\tilde{\phi}}{\partial r}, \quad (3)$$

$$\frac{d\varphi}{dt} = \frac{v_\parallel(r)}{R_0}. \quad (4)$$

The wave and frequency spectra of drift instabilities can be obtained from experimental data. We suppose that there is a broad spectrum of frequencies $\omega_n = n\omega_0$ and wave vectors, described by a Fourier expansion [24,25]

$$\tilde{\phi}(r, \theta, \varphi; t) = \sum_{m, \ell, n} \phi_{m, \ell, n} \cos(m\theta - \ell\varphi - n\omega_0 t), \quad (5)$$

where, for simplicity, the Fourier coefficients are taken as constants over the plasma region of interest. Moreover, we assume that there is a dominant Fourier mode with $m = M$ and $\ell = L$, respectively. Using Poisson sum formula we rewrite the above expression as

$$\tilde{\phi}(\theta, \varphi; t) = 2\pi \phi_{ML} \cos(M\theta - L\varphi) \sum_{n=-\infty}^{\infty} \delta(\omega_0 t - 2\pi n), \quad (6)$$

where the delta functions have been introduced so as to transform continuous-time equations into a discrete-time map.

On defining the variables $I = (r/a)^2$ and $\psi = M\theta - L\varphi$, the drift equations of motion (2)–(4) become

$$\frac{dI}{dt} = \frac{4\pi M\phi}{a^2 B} \sin \psi \sum_{n=-\infty}^{\infty} \delta(\omega_0 t - 2\pi n) = -\frac{\partial H}{\partial \psi}, \quad (7)$$

$$\frac{d\psi}{dt} = \frac{v_{\parallel}(r)}{R_0} \left(\frac{M}{q(r)} - L \right) - \frac{ME_r(I)}{aB\sqrt{I}} = \frac{\partial H}{\partial I}, \quad (8)$$

where $\phi_{ML} \equiv \phi$, and $H(I, \psi, t)$ is the corresponding Hamiltonian, describing a nonautonomous one degree-of-freedom system. Within this context, it turns out that (I, ψ) are actually action-angle variables.

A Poincaré (stroboscopic) map can be obtained [24] by defining discrete variables (I_n, ψ_n) , that represent the values of action and angle at integer multiples of the characteristic period $T = 2\pi/\omega_0$. With the definition $\Psi_n = \psi_n/(2\pi)$, there results

$$I_{n+1} = I_n + \beta \sin(2\pi \Psi_n), \quad (9)$$

$$\Psi_{n+1} = \Psi_n + \alpha v_{\parallel}(I_{n+1}) \left(\frac{M}{q(I_{n+1})} - L \right) + \gamma \frac{E_r(I_{n+1})}{\sqrt{I_{n+1}}}, \quad (10)$$

where we define the quantities $\alpha = 1/(\omega_0 R_0)$, $\beta = 4\pi M\phi/(a^2 B\omega_0)$, and $\gamma = -M/(aB\omega_0)$.

For numerical simulations, we have taken parameters from TCABR tokamak, operating at the Physics Institute of São Paulo University (Brazil) [26]. We have normalized lengths by the tokamak minor radius $a = 0.18$ m, and magnetic field strengths by the toroidal field intensity at the axis $B_0 = 1.1$ T. The external electric field is normalized with respect to its value at plasma edge E_0 , such that velocities are normalized according to the factor $v_0 = E_0/B_0$ and use the factor $t_0 = a/v_0$. Finally, the intensity of the potential associated with drift instabilities is normalized to $\phi_0 = a_0 E_0$.

In addition, we must specify the action dependence of the safety factor $q(I)$, electric field $E_r(I)$, and the toroidal velocity $v_{\parallel}(I)$. We have used the following expressions, compatible with profiles measured in the TCABR tokamak [26]:

$$q(I) = q_1 + q_2 I^2 + q_3 I^3, \quad (11)$$

$$E_r(I) = e_1 I + e_2 \sqrt{I} + e_3, \quad (12)$$

$$v_{\parallel}(I) = v_1 + v_2 \tanh(v_3 I + v_4), \quad (13)$$

where the normalized values of the various coefficients are in Table I. In the following numerical simulations we will keep fixed all quantities, except the normalized value of the perturbation strength β , which we will take as our variable parameter, representing the intensity of the perturbation. Indeed,

TABLE I. Normalized parameter values for the two-dimensional drift map.

q_1	5.0	e_3	4.13	M	15
q_2	-6.3	v_1	-9.867	L	6
q_3	6.3	v_2	17.47	ω_0	16.36
e_1	10.7	v_3	10.1	α	1.83×10^{-2}
e_2	-15.8	v_4	-9.00	γ	-9.16×10^{-1}

for $\beta = 0$ the map reduces to a nontwist radial map, due to the nonmonotonicity of the profiles used in this paper, compatible with the formation of internal transport barriers [27].

In Fig. 1, we showed the phase spaces for the map (9)–(10). The increase of β causes the breaking of KAM curves and the chaotic region expands to internal regions of the plasma.

III. CHAOTIC SADDLE AND THEIR INVARIANT MANIFOLDS

In this section we will discuss the problem of (passive) particle escape in the $\mathbf{E} \times \mathbf{B}$ flow as an open nonintegrable Hamiltonian system. For simplicity, let us denote by \mathbf{M}_{β} the discrete map (9)–(10),

$$(I_{n+1}, \Psi_{n+1}) = \mathbf{M}_{\beta}(I_n, \Psi_n),$$

where the subscript β stands for the control parameter, proportional to the intensity ϕ of the electrostatic fluctuations acting upon the impurity plasma particles. All other map parameters are being fixed at constant values. We will consider values of the control parameter β such that there is a wide chaotic region near the boundary line $I = 1$, which is an analog for a tokamak wall. Hence, any map orbit for which $I_n \geq 1$ is considered as an escaping orbit and is removed from the computation. In this way we transform our Hamiltonian system into an open one.

As a general rule, any particle, which initial condition belongs to this chaotic region will wander erratically and eventually escape out of the system by colliding with the wall at $I = 1$. However, there are nonescaping orbits even in the chaotic region, for very special initial conditions. An example are the unstable periodic orbits embedded in the chaotic sea. In general, all the nonescaping orbits are unstable and the union of all nonescaping orbits forms a Cantor-like set of Lebesgue measure zero.

Although this set of nonescaping orbits is rather exceptional, it influences the motion of particles in its neighborhood: A typical initial condition generates an orbit, which follows closely some unstable periodic orbit for a given time, and then it jumps to the proximity of another periodic orbit and so on. This wandering among nonescaping periodic orbits ultimately yields chaotic particle motion. As a consequence, these orbits have positive average Lyapunov exponent λ .

A chaotic saddle is an invariant, nonattracting chaotic set formed by the union of all nonescaping particle trajectories in the chaotic orbit. The chaotic saddle is a fractal object with (box-counting) dimension D'_0 [28]. Each nonescaping orbit belonging to a chaotic saddle has a stable and an unstable manifold. These manifolds are fractal curves with a complicated structure already described by Poincaré

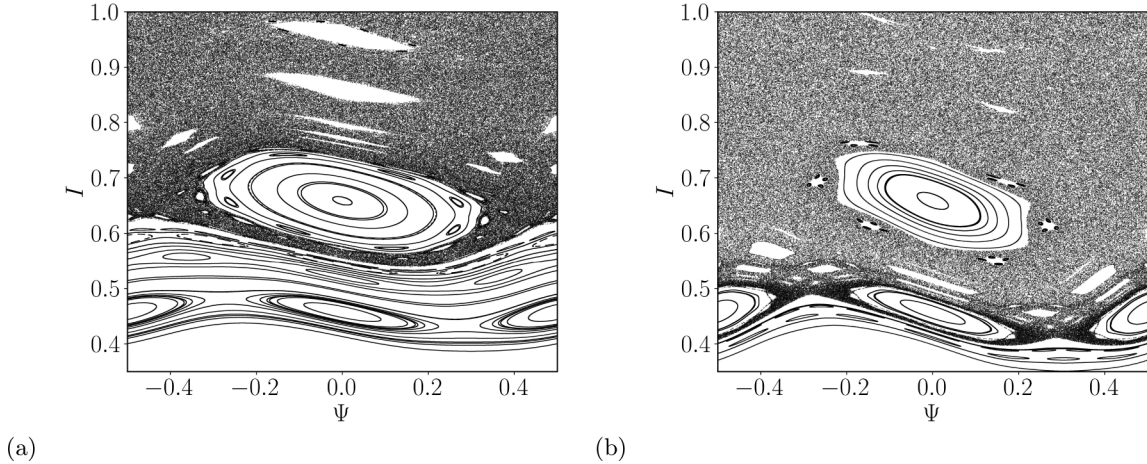


FIG. 1. Phase spaces of the map with the profiles and parameters for TCABR, with (a) $\beta = 0.05$ and (b) $\beta = 0.08$.

(homoclinic tangle), with dimension D_0 . In a Hamiltonian system, due to time-reversal invariance, the stable and unstable invariant manifolds have identical fractal dimension, such that $D'_0 = 2(D_0 - 1)$.

In a two-dimensional phase space, as for the map \mathbf{M}_β , we observe that the invariant manifold dimension is $1 < D_0 < 2$, such that the chaotic saddle dimension is $0 < D'_0 < 2$. In physical terms, let us consider a bunch of particles (passive tracers), which overlaps with the stable manifold of the chaotic saddle. In the Poincaré surface of section this bunch of particles can be represented by a droplet advected by the $\mathbf{E} \times \mathbf{B}$ drift flow of the plasma. As we iterate the map \mathbf{M}_β a large number of times, the droplet shape is modified such that it approaches the chaotic saddle with time (measured in map iterations).

Within this deformed droplet, however, only a small number of particles fall close enough to the stable manifold of the chaotic saddle. The remaining particles escape away along the unstable manifold of the chaotic saddle, i.e., passive particles trace out the invariant unstable manifold after a large enough time, until they eventually escape by reaching the tokamak wall at $I = 1$. Approximations of the invariant manifolds can be obtained with the sprinkler method [29]. A bounded region \mathcal{A} of the phase space is divided by a grid of points (Ψ_0, I_0) that are iterated m times. If the values of (Ψ_m, I_m) remain inside \mathcal{A} , then the m th iterates are numerical approximations of the unstable manifold. The initial conditions (Ψ_0, I_0) will be approximations of the stable manifold. Moreover, the $(m/2)$ -th iterates are a numerical approximation of the chaotic saddle. In the Figs. 2(a) and 2(b) we show the stable and unstable manifolds, respectively, for the map (9)–(10) using a grid of 1000×1000 initial conditions in the rectangle $-0.5 \leq \Psi \leq 0.5$, $0.8 \leq I \leq 1.0$ with $m = 10$. In Fig. 2(c) it is shown the chaotic saddle formed by the intersection of the manifolds.

The invariant stable manifold of the chaotic saddle is also physically relevant. In the case where exits are present, the sets of initial conditions (I_0, Ψ_0) (in the Poincaré surface of section) leading to trajectories escaping through exits are the corresponding escape basins. In a previous paper [14], we showed that the boundary of these escape basins is the closure of the invariant stable manifold of the chaotic saddle. Hence, for time large enough, the dimension of the escape

basin boundary is a good numerical approximation for the dimension of the invariant stable manifold D_0 . We can estimate the latter using the box counting method [30]. The box counting dimension was calculated considering that the area of interest is formed by a regular grid of $M \times M$ points. We take two-dimensional boxes with lateral length ϵ , so that the boxes cover the area completely. We then count the number N of boxes required to cover the stable manifold. The box counting is defined as

$$D_0 = \lim_{\epsilon \rightarrow 0} \frac{\ln N(\epsilon)}{\ln(1/\epsilon)}. \quad (14)$$

The box counting dimension D_0 of the stable manifold is then obtained as the angular coefficient of the linear least squares fit (LLSF) of a first-order polynomial to the pair of points $[\ln(1/\epsilon), \ln N(\epsilon)]$, with ϵ in the interval varying 10^{-10} to 10^0 .

IV. ESCAPE RATE AND LYAPUNOV EXPONENTS

The characterization of the dynamics of area preserving maps can be done by computing the Lyapunov exponents [31,32]. For a two-dimensional map, there are two Lyapunov exponents λ_1 and λ_2 , and the dynamics is chaotic if one of them is positive. For area preserving maps, like (9)–(10), it is necessary that $\lambda_1 = -\lambda_2$. This makes it possible to distinguish regular orbits whose Lyapunov exponent it is zero, for infinite time, and chaotic orbits who have $\lambda_1 > 0$. The positive Lyapunov exponent will be referred to as λ_{\max} , unless specified otherwise. In Fig. 3, we plot the values of λ_{\max} for a grid of uniformly distributed initial conditions iterated by 5×10^5 times.

Within the chaotic region, the dynamics is governed by the chaotic saddle formed by the union of all nonescaping orbits. For each initial condition (I_0, Ψ_0) we have a different escape time, or the number of map iterations τ it takes for a given trajectory to reach the tokamak wall $I = 1$. Due to the presence of the chaotic saddle, this escape time strongly depends on the initial condition, so we expect a statistical distribution of escape times according to an exponential

$$P(\tau) = P_0 \exp(-\kappa\tau), \quad (15)$$

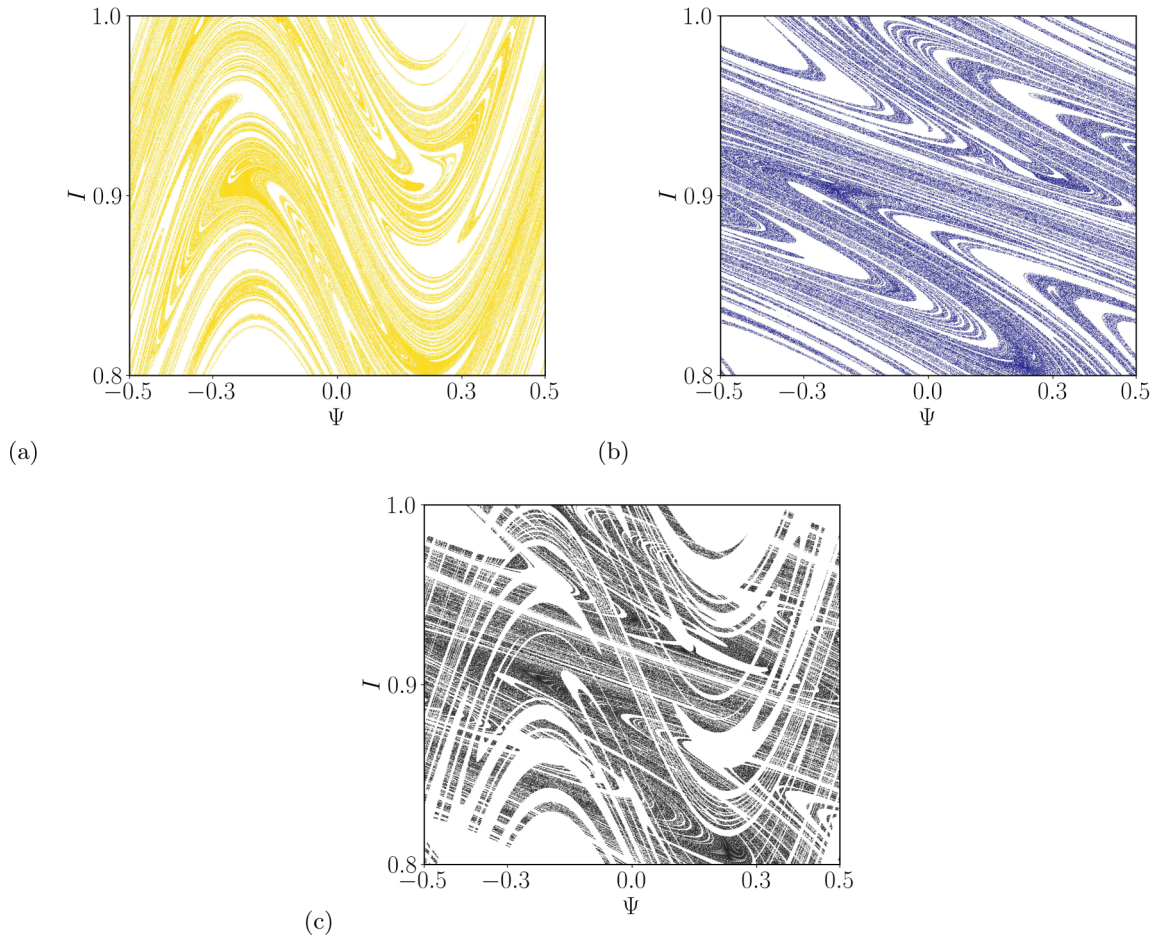


FIG. 2. In (a) the stable manifold (yellow), in (b) the unstable manifold (blue) and in (c) the chaotic saddle (black), for $\beta = 0.1$.

where P_0 is a normalization constant and $\kappa = 1/\langle \tau \rangle$ is the so-called escape rate, where $\langle \tau \rangle$ is the average escape time. In order to determine this number, we consider the sprinkler method, computing the number of initial conditions that remains inside \mathcal{A} for different values of the number of iterations

m . In Fig. 4 the number of particles in \mathcal{A} is shown as a function of time, and how this follows the Eq. (15) with $\kappa = 0.0227$. In Table II the values of κ for different values of β are shown.

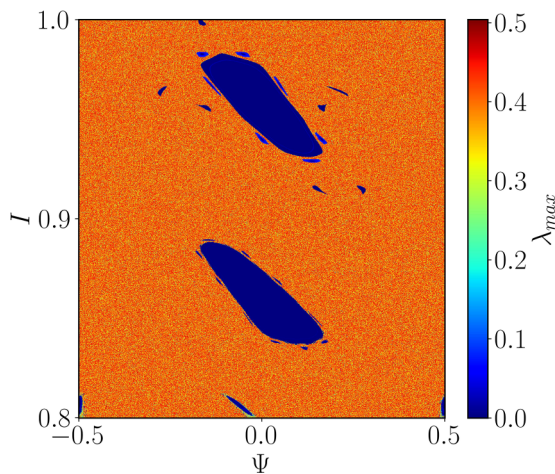


FIG. 3. Color map for the maximum Lyapunov exponent, for a grid of 1000×1000 initial conditions, uniformly distributed in the phase space for $\beta = 0.05$.

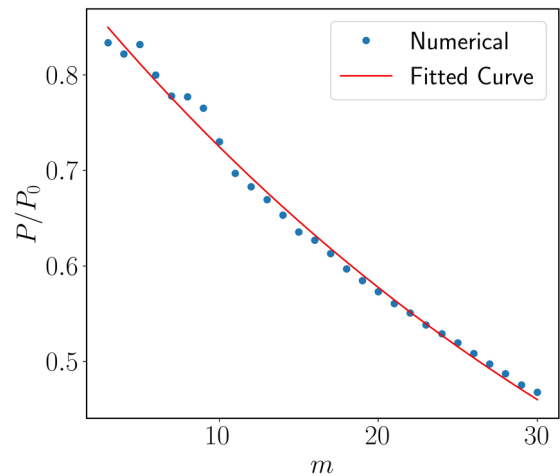


FIG. 4. Number of particles that remain inside a bounded region \mathcal{A} of the phase space, as a function of the time of iterate, for $\beta = 0.08$. The red line is the fit from which we obtain the escape rate, and the blue dots are from the numerical simulation.

TABLE II. Results for the escape rate (κ), maximum Lyapunov exponent (λ_{\max}), information dimension (D_1), and box counting dimension (D_0), respectively, as a function of the perturbation amplitude β .

β	κ	λ_{\max}	D_1	D_0
0.05	0.0044 ± 0.0003	0.50 ± 0.12	1.99	1.99
0.06	0.0092 ± 0.0003	0.50 ± 0.09	1.98	1.99
0.07	0.0148 ± 0.0005	0.51 ± 0.08	1.97	1.99
0.08	0.0227 ± 0.0004	0.53 ± 0.07	1.96	1.99
0.09	0.0236 ± 0.0005	0.54 ± 0.07	1.96	1.97
0.10	0.0412 ± 0.0008	0.60 ± 0.07	1.93	1.96
0.11	0.037 ± 0.001	0.61 ± 0.08	1.94	1.96
0.12	0.065 ± 0.001	0.64 ± 0.08	1.90	1.96

There is a general relation, valid for transient chaos, involving the information dimension D_1 of the invariant manifolds, the average Lyapunov exponent λ around the chaotic saddle, and the escape rate $\kappa < \lambda$ of particles in the chaotic sea of a two-dimensional phase space, namely

$$D_1 = 2 - \frac{\kappa}{\lambda}. \quad (16)$$

To derive this expression, we cover the portion of the invariant unstable manifold in the two-dimensional phase space with boxes of sidelength ϵ . The union of all those boxes form a plane figure of area \mathcal{A} .

After τ iterations of the map \mathbf{M} , taking as initial conditions a large number of points belonging to the set of boxes, a number of particles will escape through the exit $I = 1$. Hence the the area \mathcal{A}' occupied by the nonescaping particles will be smaller by a factor of $\exp(-\kappa\tau)$, with respect to the initial area \mathcal{A} .

The new area \mathcal{A}' refers to a closed contour that has been shrunk along the stable invariant manifold, towards the unstable invariant manifold. Using the definition of box-counting dimension, we now cover the region of area \mathcal{A}' with boxes of sidelength $\epsilon' = \epsilon \exp(-\lambda\tau)$, where $-\lambda$ is the average negative Lyapunov exponent of orbits escaping off but near the unstable invariant manifold.

A cautionary remark: we consider this new covering of boxes, which are typical with respect to the natural measure on the chaotic saddle. In this case we are, strictly speaking, dealing with the information dimension D_1 of the invariant manifold, which takes into account most of the natural measure of nonescaping orbits belonging to the chaotic saddle. Hence the number of boxes necessary to cover \mathcal{A}' scales as $N(\epsilon) \sim \epsilon^{-D_1}$. In general, it turns out that $D_1 \leq D_0$, i.e., the fractal dimension D_0 of the invariant manifolds is an upper bound to the information dimension D_1 . In practice, if we choose a typical set of boxes, D_1 is very close to D_0 and provides a good estimate of D_0 . By multiplying the number of boxes by the area of each two-dimensional box, the total area is initially $\mathcal{A} \sim N(\epsilon)\epsilon^2 \sim \epsilon^{2-D_1}$. After τ map iterations one has

$$(\epsilon e^{-\lambda\tau})^{2-D_1} \sim \epsilon^{2-D_1} e^{-\kappa\tau},$$

resulting in Eq. (16).

Another useful characterization of the chaotic saddle is provided by the topological entropy K_0 , defined (in the present context) as follows: let $L(t)$ be the perimeter length of a closed region bounding a number of passive particles in the Poincaré section of the phase space. It increases with time as $e^{K_0 t}$, where t is measured in number of map iterations. K_0 is an upper bound to the metric entropy $K_1 = \lambda_{\max} - \kappa$. For a closed system $\kappa = 0$ and $K_0 \leq K_1 = \lambda > 0$.

Table II shows the values of the information dimension, calculated with the Eq. (16), and the box counting dimension, for various values of the parameter β . Both dimensions are very close to the dimension of the phase space itself. These results point that the chaotic saddle structure is an extreme fractal. Moreover, for all studied values, the relation $D_1 \leq D_0$ is true, and there is small variation of the dimensions with the respect the parameter β .

V. RECURRENCE TIME ENTROPY

One of the distinctive features of the maximal Lyapunov exponents depicted in Fig. 3 is the nonuniformity of the large chaotic region obtained for perturbation amplitude large enough. There is a range of values of the positive Lyapunov exponent λ , indicating that there are segments of the chaotic orbit, which are trapped in the vicinity of periodic islands for some time, before escaping out to the large chaotic region with higher values of λ . This phenomenon, called *stickiness*, has been described for quite a long time in numerical investigation of Hamiltonian systems, in both discrete and continuous time [22].

The reason for this sticky behavior of a chaotic orbit near a periodic island is the existence of perforated tori, or cantori, which act as a transport barrier for a limited time only, although this trapping time can be arbitrarily long depending on the size of the holes [33]. Nevertheless, such a trapping interferes in long-time calculations such as those necessary to compute the Lyapunov exponent. Hence the quantitative characterization of sticky behavior is necessary to evaluate the extent of such influence on time averages of dynamical quantities.

One possible characterization is the distribution of finite-time Lyapunov exponents $P(\lambda_n)$, which are computed over time- n sections of a single, long chaotic orbit. Such finite-time exponents depend on the initial condition (I_0, Ψ_0) , unlike its infinite-time counterpart $\lambda = \lim_{n \rightarrow \infty} \lambda_n(I_0, \Psi_0)$. While there is a main peak in this statistical distribution centered at λ , the sticky behavior causes a second peak near zero [34].

Recently, concepts based on recurrence plots have been developed to characterize stickiness [23,35,36]. Recurrence plots [37] (RP) are graphical representations of the recurrence matrix for a time series. We use the shorthand notation $\mathbf{x}_n = (I_n, \Psi_n)$ to denote the current values of the action-angle variables for the particle position in the Poincaré surface of section. Accordingly, given a time series from a chaotic orbit $\mathbf{x}_i \in \mathbb{R}$ ($i = 1, 2, \dots, N$), the corresponding recurrence matrix elements are defined as

$$R_{ij} = \mathcal{H}(\epsilon - \|\mathbf{x}_i - \mathbf{x}_j\|), \quad (17)$$

where N is the length of the time series, \mathcal{H} is the Heaviside function, and $\|\mathbf{x}_i - \mathbf{x}_j\|$ is the spatial distance between

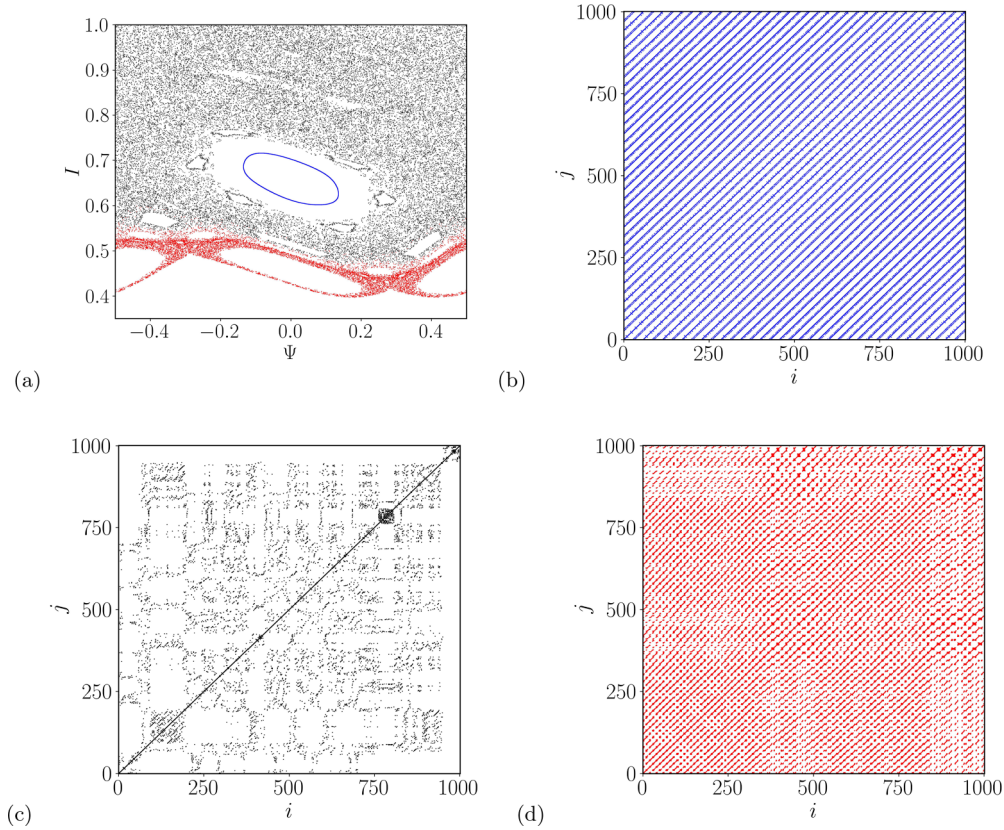


FIG. 5. (a) Phase space of a quasiperiodic orbit (blue), a chaotic orbit (black), and a sticky orbit (red) of the map with $\beta = 0.08$ iterated for $N = 1000$ times. Recurrence matrix of (b) the quasiperiodic orbit, (c) the chaotic orbit, and (d) the sticky orbit.

two states, here calculated with the supremum (or maximum) norm. An Euclidean norm could also be used yielding similar results.

Careful attention should be given to the choice of the threshold ε , since its value influences the results: if ε is large, we would record too many recurrences with a barely distinguishable RP. On the other hand, for a too small ε , we would barely register recurrences. A good compromise is to consider ε to be 10% of the time series standard deviation σ [38,39].

The use of the Heaviside function limits the components of RP to ones and zeros. As such RPs are a kind of contour plots with only two levels: on a recurrence it is 1, otherwise 0. Two states are recurrent when the state at the time $t = i$ is close, up to the distance ε to a different state at $t = j$, that is $\mathbf{x}_i \approx \mathbf{x}_j$. The recurrent states are represented by dots in the plot, and display various diagonal structures depending of the dynamics of the underlying system. The vertical distances between these lines correspond to different return times for points belonging to a given map orbit [36,40,41]. Recently it has been proposed that the white vertical lines of a RP could be used to detect stickiness regions [23].

In Figs. 5(a)–5(d), we show the phase space for three orbits together with their corresponding RPs for the first 1000 iterations of the drift map, for a given perturbation strength of $\beta = 0.08$. The RP for a quasiperiodic orbit, chosen inside a periodic island, cf. Fig. 5(b), consists of uninterrupted diagonal lines, characterized by having three return times [36], while a chaotic orbit shown in 5(c) exhibits short diagonal lines, and the vertical distances of the lines are not regular.

In the case of sticky orbits [Fig. 5(d)] the diagonal lines are longer than those in the chaotic case, but not as long as for the quasiperiodic case, and the vertical lines present some regularity.

It is possible to distinguish the different solutions of a nonlinear system by counting the number of return times of an orbit. If there exists a single return time then the orbit is periodic with a period equal to the return time. On the other hand, if the orbit is quasiperiodic, Slater's theorem [42–44] asserts that there are three different return times, and the third one is the sum of the previous two. Finally, if the orbit is chaotic there are more than three return times. Given that the distances between vertical lines in the RP are estimates of the recurrence times, the statistical distribution of white vertical lines can be used to distinguish these orbits.

We consider the total number of white vertical lines of length ν , as given by the histogram

$$P_w(\nu) = \sum_{i,j=1}^N R_{ij} R_{ij+\nu} \prod_{k=0}^{\nu-1} (1 - R_{ij+k}). \quad (18)$$

Let N_w be the total number of white vertical line segments. Then the probability of a white vertical line of length ν is $p_w(\nu) = P_w(\nu)/N_w$. From the latter we can define the recurrence time entropy (S_{RT}) as Shannon's entropy for white vertical lines, as [23]

$$S_{RT} = - \sum_{\nu=\nu_{\min}}^{\nu_{\max}} p_w(\nu) \ln p_w(\nu), \quad (19)$$

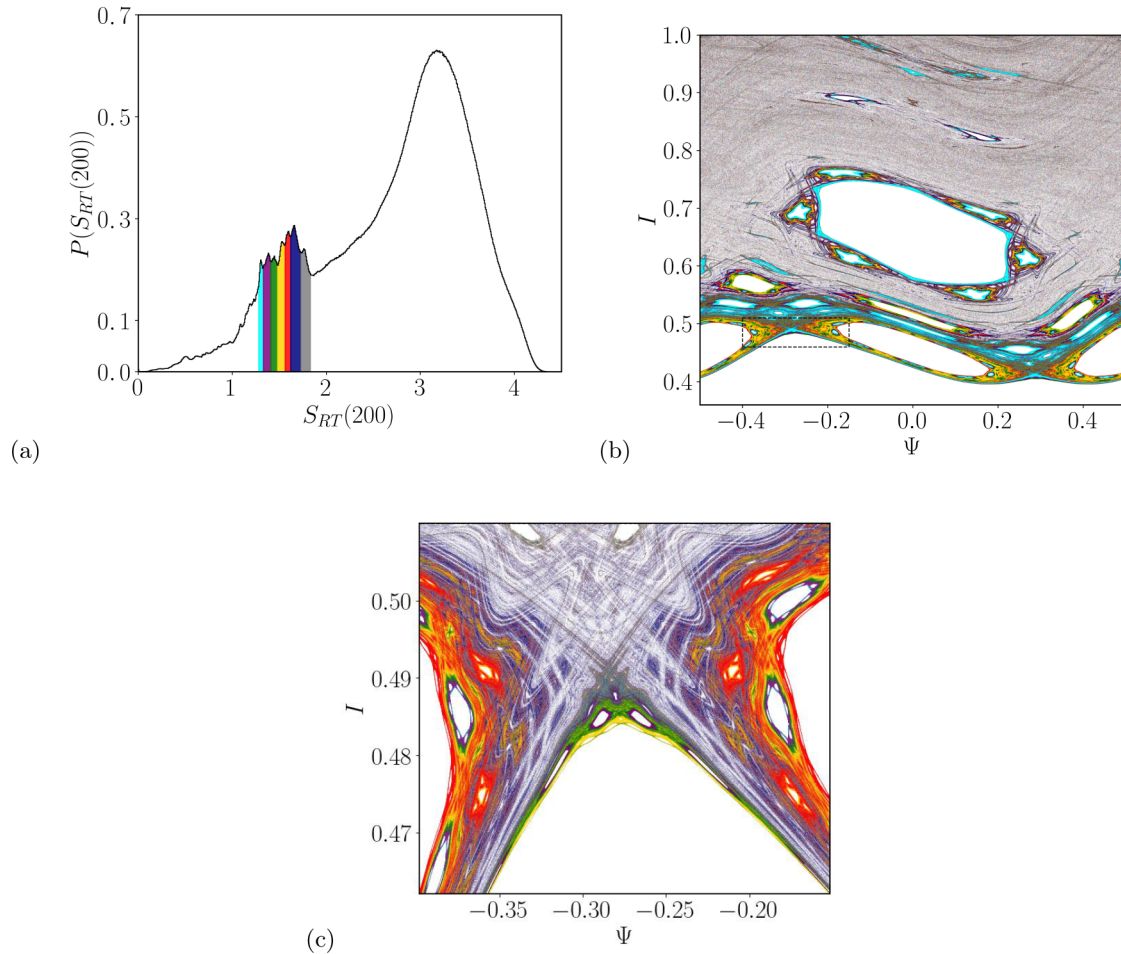


FIG. 6. (a) Finite-time S_{RT} distribution for a single chaotic orbit, with $n = 200$, $N = 10^{10}$, and $\beta = 0.08$. (b) The phase space points that generate the minor peaks in (a). (c) A magnification of the region indicated by the black dashed lines.

where ν_{\min} and ν_{\max} are the lengths of the shortest and longest white vertical line, respectively. We consider $\nu_{\min} = 1$. The distribution of white vertical lines may be influenced by the border lines of the RP due to its finite size. To mitigate this effect, we have excluded the white vertical lines that originate and terminate at the RP's border. The S_{RT} for a periodic orbit is zero, given that it has only one return time, a quasiperiodic orbit will have a low value of S_{RT} , while a chaotic one have a larger value of S_{RT} . Therefore, chaotic orbits, which experience stickiness have smaller values of the S_{RT} than chaotic, but higher than quasiperiodic orbits.

Following the evolution of a single chaotic orbit for a long time N , the trajectory may be trapped in the stickiness region, and stay therein for a possibly long time until eventually escapes to the chaotic sea. Therefore, the transition among different regimes can be better understood considering finite time values of the S_{RT} , for $n \ll N$. Accordingly, we computed the finite time S_{RT} for a single chaotic orbit in windows of size n , $\{S_{RT}^i(n)\}_{i=1,2,\dots,M}$, where $M = N/n$ and define the probability distribution of the finite-time S_{RT} , $P(S_{RT}(n))$, by computing a frequency histogram of $\{S_{RT}^i(n)\}$ as shown in Fig. 6(a) for $N = 10^{10}$ and $n = 200$.

The observed multimodal distribution can be attributed to the intricate hierarchical islands-around-islands structure that

permeates the phase space. When an orbit finds itself within the chaotic sea, it experiences an extended time $n - S_{RT}$, leading to the highest peak in the distribution. When the orbit is trapped near an island the S_{RT} is low corresponding to smaller values in distribution. The trapped orbit may enter an inner level in the hierarchical structure, and the transition among these levels is the cause of the multimodal behavior shown in Fig. 6(a).

For a chaotic orbit far from sticky regions, the corresponding finite-time $S_{RT}(n)$ is large and is represented by the largest peak in the distribution of Fig. 6(a). If, however, a chaotic orbit is trapped into a sticky region, the distribution has smaller peaks and correspondingly smaller values of $S_{RT}(n)$. To identify the regions in phase space corresponding to the peaks in the distribution, we monitor the time series of $S_{RT}(200)$ and generate a plot, Fig. 6(b), that displays 200 phase space positions (Ψ, I) using distinct colors to represent various ranges of $S_{RT}(200)$. The different peaks are related to the different hierarchical levels of the structure. Figure 6(c) presents a magnification of the structures.

We remark that stickiness is actually a transient phenomenon: an initially sticky orbit will eventually become a full-fledged chaotic orbit. Before that occurs, however, the orbit visits different sticky regions according to the

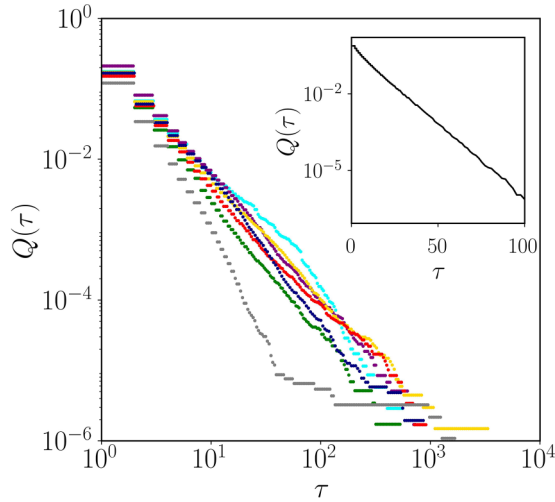


FIG. 7. log - log plot of $Q(\tau)$ for each sticky region, with $N = 10^{10}$ and $n = 200$. (Inset) log-linear plot of $Q(\tau)$ of the phase space points belonging to the biggest peak in Fig. 6(a). The colors of the dots correspond to the colors of Fig. 6(a).

hierarchical structure of islands-around-islands that we have described using the histogram of finite-time S_{RT} . The time a sticky orbit spends in the vicinity of a given island is called trapping time and, as the sticky orbit visits different islands we have a sequence of trapping times $\{t_1, t_2, \dots, t_{N_t}\}$, where N_t is the total number of different trapping times. Now let us consider only those trapping times higher than a given value τ , denoted as N_τ . Hence, we can either describe the trapping times for their probability distribution $P(t)$ or by their cumulative distribution

$$Q(\tau) = \sum_{t > \tau} P(t) = \frac{N_\tau}{N_t}. \quad (20)$$

The cumulative distribution of trapping times is expected to decay with τ in different fashions according to the local dynamics. For chaotic orbits, $Q(\tau)$ decays exponentially with time, whereas sticky orbits present a power-law decay. We have numerically verified both scalings, our results being depicted in Fig. 7, where we plot the cumulative distribution as a function of τ for time-200 S_{RT} computed from a very long ($N = 10^{10}$) chaotic orbit. Different colors represent sticky orbits around the islands corresponding to Fig. 6. As a general trend, in all cases the decay is of a power-law type. We thus have an exponential decay with a fat tail characteristic of sticky behavior for all cases considered, while the decay is exponential [see the inset of Fig. 7] for the largest peak in histogram Fig. 6(a) corresponding to the hyperbolic region of the phase space.

VI. CONCLUSIONS

Chaotic saddles are invariant nonattracting chaotic sets appearing in both dissipative and conservative systems, and can be thought as the backbone of the aperiodic behavior. In open conservative systems, the chaotic saddle underlies the dynamics of escape, and there are some observable manifestations of this presence. In this paper we illustrated the role of

the chaotic saddle in the impurity particle escape in a toroidal plasma under the simultaneous action of magnetic and electric fields, as well as an overall toroidal velocity. All these factors have been taken into account to describe impurity particle escape in realistic regimes of a tokamak operation. In spite of this, the model has considered a number of simplifications that reduce the number of variable parameters, without removing the basic physical processes involved.

We have considered electric fields resulting from low-frequency electrostatic fluctuations related to drift instabilities in toroidal plasmas. The $\mathbf{E} \times \mathbf{B}$ drift motion has all the features of a nonintegrable area-preserving system, in a Poincaré surface of section. In particular, for sufficiently large values of the fluctuation amplitude there is a wide chaotic orbit near the tokamak wall.

The chaotic saddle can be thought as the set of intersections between the stable and unstable invariant manifolds of some unstable periodic orbit embedded in the chaotic orbit. By allowing particles to escape through the tokamak wall, the system reduces to an open Hamiltonian system, and we can then investigate the dynamical properties of chaotic particle escape. Any particle starting from an initial position off but very near to the chaotic saddle will closely follow the corresponding unstable invariant manifold until it reaches the tokamak wall and is considered lost, being removed from numerical integration of the model. Hence the unstable manifolds provide escape channels for the particles to exit the tokamak. Since the chaotic saddle is itself a fractal Cantor-dust-like set, we expect that this fractal nature will also be present in the distribution of impurity particles hitting the tokamak wall. This has potential importance for the design of devices aiming to reduce or control plasma-wall interactions like divertors or limiters.

The presence of a chaotic saddle in the chaotic region leads to an exponential distribution for the escape time of particles through the tokamak wall. The information dimension of the invariant manifolds can be estimated by the computation of the corresponding escape rate and the average Lyapunov exponent. Our results show that the information and box-counting dimensions both decrease with the intensity of electrostatic fluctuations. Another observable influence of the chaotic saddle is the fractal character of escape basin boundaries. If we divide the tokamak wall into two or more partitions, we can assign to each of them a set of initial conditions such that particles will eventually escape through that exit, or its escape basin. In this case the escape basin boundary is a fractal, whenever pieces of it intersect the stable invariant manifold of the chaotic saddle. Hence we can summarize the role of the chaotic saddles in the chaotic particle escape by the following: (i) the unstable manifold provides escape channels, (ii) the stable manifold indicates the fractality of escape basin boundaries.

Using the concept of recurrence time entropy (S_{RT}), our analysis reveals the presence of the stickiness effect within the system and quantifies its strength. This phenomenon entails chaotic orbits becoming temporarily trapped in the vicinity of periodic islands before eventually escaping into the chaotic region. Notably, the finite-time S_{RT} distribution exhibits a multimodal pattern. While the major peak

corresponds to the chaotic sea, there are a number of minor peaks corresponding to a distinct hierarchical level within the islands-around-islands structure. Consequently, it becomes feasible to distinguish the various hierarchical levels inherent to this complex structure. Moreover, it is possible to calculate the cumulative distribution of the trapping times related to each hierarchical level. We have shown that the largest peak corresponds to the hyperbolic region of the chaotic phase space, such that the cumulative distribution of trapping times exhibits an exponential decay, whereas the trapping times associated to the smaller peaks in this distribution exhibit a power-law tail, which is a characteristic feature of the stickiness effect.

ACKNOWLEDGMENTS

The authors would like to thank the anonymous referees who provided useful and detailed comments on an earlier version of the manuscript. The authors thank the financial support from the Brazilian Federal Agencies (CNPq) under Grants No. 407299/2018-1, No. 302665/2017-0, No. 403120/2021-7, No. 311168/2020-5, No. 140713/2020-4, and No. 301019/2019-3; the São Paulo Research Foundation (FAPESP, Brazil) under Grants No. 2018/03211-6, No. 2022/12736-0, and No. 2022/04251-7 and support from Coordenação de Aperfeiçoamento de Pessoal de Nível Superior (CAPES) under Grant No. 88887.485462/2020-00.

-
- [1] C. Angioni, *Plasma Phys. Control. Fusion* **63**, 073001 (2021).
- [2] D. E. Post and R. Behrisch, *Introduction to the Physics of Plasma-Wall Interactions in Controlled Fusion* (Plenum Press, New York, 1986).
- [3] W. Horton and S. Benkadda, *ITER Physics* (World Scientific, Singapore, 2015).
- [4] AEA ITER Technical Basis, ITER EDA Documentation Series No. 24 (International Atomic Energy Agency, Vienna, 2002).
- [5] G. Federici, P. Andrew, P. Barabaschi, J. Brooks, R. Doerner, A. Geier, A. Herrmann, G. Janeschitz, K. Krieger, A. Kukushkin *et al.*, *J. Nucl. Mater.* **313**, 11 (2003).
- [6] T. E. Evans, C. Chandre, X. Leoncini, and G. Zalavsky, *Chaos, Complexity and Transport: Theory and Applications: Proceedings of the CCT'07, Marseille, France, 4-8 June 2007* (World Scientific, Singapore, 2008).
- [7] E. Bertolini, G. Celentano, J. R. Last, J. Tait, A. Tesini, G. D. Mut, C. D'Urzo, L. Ghirlanda, A. Laurenti, A. Maragliano, and A. Veardo, *IEEE Trans. Magn.* **28**, 275 (1992).
- [8] B. Lipschultz, B. LaBombard, J. L. Terry, C. Boswell, and I. H. Hutchinson, *Fusion Sci. Technol.* **51**, 369 (2007).
- [9] F. Karger and K. Lackner, *Phys. Lett. A* **61**, 385 (1977).
- [10] R. L. Viana, *Chaos Solit. Fractals* **11**, 765 (2000).
- [11] T. J. Martin and J. B. Taylor, *Plasma Phys. Control. Fusion* **26**, 321 (1984).
- [12] M. W. Jakubowski, T. E. Evans, M. E. Fenstermacher, M. Groth, C. J. Lasnier, A. W. Leonard, O. Schmitz, J. G. Watkins, T. Eich, W. Fundamenski *et al.*, *Nucl. Fusion* **49**, 095013 (2009).
- [13] A. Punjabi, H. Ali, and A. Boozer, *Phys. Plasmas* **4**, 337 (1997).
- [14] L. C. Souza, A. C. Mathias, I. L. Caldas, Y. Elskens, and R. L. Viana, *Chaos* **33**, 083132 (2023).
- [15] A. C. Mathias, G. Perotto, A. B. Schelin, I. L. Caldas, and R. L. Viana, *Int. J. Bifurc. Chaos* **32**, 2250078 (2022).
- [16] T. E. Evans, R. A. Moyer, J. G. Watkins, P. R. Thomas, T. H. Osborne, J. A. Boedo, M. E. Fenstermacher, K. H. Finken, R. J. Groebner, M. Groth *et al.*, *J. Nucl. Mater.* **337**, 691 (2005).
- [17] T. E. Evans, R. K. W. Roeder, J. A. Carter, and B. I. Rapoport, *Contrib. Plasma Phys.* **44**, 235 (2004).
- [18] I. L. Caldas and H. Tasso, *Plasma Phys.* **20**, 1299 (1978).
- [19] R. J. Goldston, *Introduction to Plasma Physics* (CRC, Boca Raton, FL, 2020).
- [20] W. Horton, *Plasma Phys. Control. Fusion* **27**, 937 (1985).
- [21] J. Weiland and A. Zavorodny, *Rev. Mod. Plas. Phys.* **3**, 8 (2019).
- [22] G. Contopoulos and M. Harsoula, *Int. J. Bifurc. Chaos* **18**, 2929 (2008).
- [23] M. R. Sales, M. Mugaine, J. D. Szezech Jr., R. L. Viana, N. Marwan, and J. Kurths, *Chaos* **33**, 033140 (2023).
- [24] W. Horton, H.-B. Park, J.-M. Kwon, D. Strozzi, P. J. Morrison, and D.-I. Choi, *Phys. Plasmas* **5**, 3910 (1998).
- [25] F. A. Marcus, I. L. Caldas, Z. O. Guimarães-Filho, P. J. Morrison, W. Horton, Y. K. Kuznetsov, and I. C. Nascimento, *Phys. Plasmas* **15**, 112304 (2008).
- [26] I. C. Nascimento, Y. K. Kuznetsov, J. H. Severo, A. M. Fonseca, A. Elfimov, V. Bellintani, M. Machida, M. V. A. P. Heller, R. M. O. Galvão, E. K. Sanada, and J. I. Elizondo, *Nucl. Fusion* **45**, 796 (2005).
- [27] L. A. Osorio, M. Roberto, I. L. Caldas, R. L. Viana, and Y. Elskens, *Phys. Plasmas* **28**, 082305 (2021).
- [28] K. Falconer, *Fractal Geometry: Mathematical Foundations and Applications* (John Wiley & Sons, Hoboken, NJ, 2004).
- [29] H. Kantz and P. Grassberger, *Physica D* **17**, 75 (1985).
- [30] K. T. Alligood, T. D. Sauer, J. A. Yorke, and D. Chillingworth, *SIAM Rev.* **40**, 732 (1998).
- [31] A. Wolf, J. B. Swift, H. L. Swinney, and J. A. Vastano, *Physica D* **16**, 285 (1985).
- [32] J. P. Eckmann and D. Ruelle, *Rev. Mod. Phys.* **57**, 617 (1985).
- [33] J. D. Meiss, *Chaos* **25**, 097602 (2015).
- [34] J. D. Szezech Jr., S. R. Lopes, and R. L. Viana, *Phys. Lett. A* **335**, 394 (2005).
- [35] M. S. Palmero, I. L. Caldas, and I. M. Sokolov, *Chaos* **32**, 113144 (2022).
- [36] Y. Zou, M. Thiel, M. C. Romano, and J. Kurths, *Chaos* **17**, 043101 (2007).
- [37] J. P. Eckmann, S. O. Kamphorst, and D. Ruelle, *Europhys. Lett.* **4**, 973 (1987).
- [38] N. Marwan, M. C. Romano, M. Thiel, and J. Kurths, *Phys. Rep.* **438**, 237 (2007).
- [39] M. Thiel, M. C. Romano, J. Kurths, R. Meucci, E. Allaria, and F. T. Arecchi, *Physica D* **171**, 138 (2002).
- [40] Y. Zou, D. Pazó, M. C. Romano, M. Thiel, and J. Kurths, *Phys. Rev. E* **76**, 016210 (2007).
- [41] E. J. Ngamga, D. V. Senthilkumar, A. Prasad, P. Parmananda, N. Marwan, and J. Kurths, *Phys. Rev. E* **85**, 026217 (2012).
- [42] N. B. Slater, *Math. Proc. Cambridge Philos. Soc.* **46**, 525 (1950).
- [43] N. B. Slater and B. Noel, *Math. Proc. Cambridge Philos. Soc.* **63**, 1115 (1967).
- [44] D. H. Mayer, *Lett. Math. Phys.* **16**, 139 (1988).